Ab initio prediction of temperature-dependent stability of heterogeneous B19' phase in TiNi alloy using atomistically informed Eshelby's ellipsoidal inclusion

Akio Ishii*

Department of Mechanical Science and Bioengineering, Osaka University, Osaka 560-8531, Japan

Abstract

In this study, we energetically predicted the temperature-dependent stability of the heterogeneous B19' phase in the B2 matrix of TiNi alloys using density functional theory (DFT) and phonon analysis informed Eshelby's ellipsoidal inclusion. The temperature-dependent eigenstrains and elastic constants for Eshelby's ellipsoidal inclusion were calculated using DFT and phonon analysis under a quasi-harmonic approximation. The stable orientation of the disk-shaped B19' phase in the B2 matrix and its total strains were evaluated with respect to temperature using Eshelby's ellipsoidal inclusion analysis. Using the total strains, the elastically deformed atomic structure of the heterogeneous B19' phase in the B2 matrix was determined, and its temperature-dependent free energy was calculated using DFT calculations and phonon analysis. Comparing the temperature-dependent free energies of the B2 and elastically deformed B19' structures, we successfully predicted that the transformation between the two phases occurs at 300 K, which agrees with experimental observations. Moreover, it is shown that the temperature-dependent difference in the elastic constants between the B19' phase and B2 matrix influences the phase transformation, which is the origin of the shape-memory effect of TiNi alloy.

Keywords: Shape memory alloy, Density functional theory, Eshelby's ellipsoidal inclusion

*Corresponding author
Email address: ishii@me.es.osaka-u.ac.jp (Akio Ishii)

1. Introduction

Shape memory alloys (SMAs) are capable of reverting to their original undeformed state upon heating above a certain characteristic temperature, i.e., they have a shape-memory effect. In addition to this, they are generally known to exhibit superelasticity, which implies that plastically deformed SMAs recover their shape once the external load is removed. Owing to these properties, SMAs are promising materials for a wide range of industrial application: structural and biomedical materials, actuators, transducers, and sensors [1]. Previous studies have revealed that the shape memory effect (superelasticity) is due to the SMA's high phase transformability with respect to heat (external load), from the matrix (parent) phase to the secondary (twin) phase, and vice versa [1]. Despite this, a detailed mechanism of the SMA deformation process remains unclear.

The near-equiatomic TiNi SMA [2] was observed to transform from a cubic B2 matrix to a monoclinic B19' secondary phase. The B19' phase is known to be the most stable secondary phase at room temperature [3–5]. The shape memory effect of the TiNi alloy is due to the reverse phase transformation from the B19' to B2 matrix at high temperatures, and the superelasticity is due to the forward or backward twinning deformation of the B19' phase [6]. Thus, to reveal the origin of the shape memory effect of this alloy, the mechanism of the phase transformation from B2 to B19' must be clarified. Many theoretical studies on this mechanism, especially using atomistic simulations, have been performed [7–18]. Although few molecular dynamics (MD) studies using empirical interatomic potential investigated the dynamics of phase transformation [12, 16, 18], majority of the studies based on density functional theory (DFT) calculations discuss the stability of the B19' structure by comparing its free energy or potential energy with that of B2 and other metastable atomic structures [7, 9–11, 13–15, 17]. Despite these efforts, the stability of the B19' phase with respect to temperature remains unclear because of the discrepancy between theoretical and experimental observations. For example, Haskins et al. calculated the temperature-dependent free energies of B2 and B19' structures using DFT-MD phase space sampling and predicted that the phase transformation temperature of the B19' phase was 500600 K, which is considerably higher than the martensite start (Ms) temperature observed experimentally ($\sim$ 300 K) [3–5, 19, 20].

The aim of the present study therefore was to predict the temperature-dependent stability of the B19' phase that is comparable with the experi-

mental observations. We believe that the existing discrepancy is due to the heterogeneity of B19' phase in real TiNi alloys, which was not considered in conventional DFT calculations because it significantly increases the computation cost, as it requires a very large atomic model to account for such heterogeneities. By combining DFT atomistic and micromechanical [21] elastic analyses, we investigated the temperature-dependent stability of the B19' phase in B2 matrix while accounting for its heterogeneity. In particular, considering heterogeneous B19' phase in B2 matrix as Eshelby's ellipsoidal inclusion, which temperature-dependent eigenstrains and elastic constants were calculated using DFT and phonon analysis under quasi-harmomic approximation (QHA), we predicted temperature-dependent morphology of heterogeneous B19' phase and the total strains of heterogeneous B19' phase, which describe the elastically deformed shape of heterogeneous B19' phase in B2 matrix [22, 23]. Using the total strains, we reproduced the elastically deformed B19' atomic structure and calculated its free energy using DFT and phonon analysis again. By the comparison of the free energy of the heterogeneous B19' phase with that of the B2 matrix, a parameter-free *ab initio* prediction of its temperature-dependent stability was achieved. The rest of the article details the methods and results of the DFT and micromechanical analyses.

2. DFT simulation

2.1. Methodology

Figure 1 shows the modeled structures of the B2 and B19' phases. These were structurally optimized using DFT calculations. The units of the supercells included two Ti and two Ni atoms and the coordinate system was set to $[110]_{\mathrm{B2}} - [1\bar{1}0]_{\mathrm{B2}} - [001]_{\mathrm{B2}}$. The B19' structure was achieved by shuffling both Ti and Ni atoms along $[1\bar{1}0]_{\mathrm{B2}}$ direction and $(001)_{\mathrm{B2}}[1\bar{1}0]_{\mathrm{B2}}$ shear deformation of B2 structure. The directions $[110]_{\mathrm{B2}}$ and $[1\bar{1}0]_{\mathrm{B2}}$ correspond to the lattice vectors $\boldsymbol{b}$ and $\boldsymbol{c}$ of B19'; the vector $\boldsymbol{a}$ however deviates from $[001]_{\mathrm{B2}}$ owing to the monoclinic structure of B19' [24–26]. The monoclinic angle of the B19' structure was 102.1°, which is consistent with previous DFT studies [9, 10, 27] but is larger than the experimentally obtained value of 97.9° [3]. The reason for this discrepancy, as explained from a micromechanical viewpoint in our previous work, is due to the heterogeneity of the experimentally observed B19' phase in the B2 matrix [23]. The free energy F per unit cell,

which is a function of the temperature T and strain ε_{ij}, can be described as follows:

$$F(\varepsilon_{11},\varepsilon_{22},\varepsilon_{33},\varepsilon_{23},\varepsilon_{31},\varepsilon_{12},T) \equiv E^{\mathrm{ele}}(\varepsilon_{11},\varepsilon_{22},\varepsilon_{33},\varepsilon_{23},\varepsilon_{31},\varepsilon_{12}) + E^{\mathrm{pho}}(\varepsilon_{11},\varepsilon_{22},\varepsilon_{33},\varepsilon_{23},\varepsilon_{31},\varepsilon_{12},T),$$
$$E^{\mathrm{pho}} = \int_0^\infty \rho(\omega,\varepsilon_{11},\varepsilon_{22},\varepsilon_{33},\varepsilon_{23},\varepsilon_{31},\varepsilon_{12}) \left(\frac{1}{2}\hbar\omega + k_{\mathrm{B}}T \ln\left[1-\exp\left(-\frac{\hbar\omega}{k_{\mathrm{B}}T}\right)\right]\right) \mathrm{d}\omega, \tag{1}$$

where E^{ele} is the energy due to electric interaction and can be calculated using conventional DFT calculations; and E^{pho} is the energy due to the vibrational entropy of phonons, which can be calculated using density functional perturbation theory (DFPT) [28]; ω is the phonon frequency; ρ is the phonon density of states; k_{B} is the Boltzmann constant; and $\hbar$ is the reduced Planck constant. In this study, we calculated $F(\varepsilon_{11},\varepsilon_{22},\varepsilon_{33},\varepsilon_{23},\varepsilon_{31},\varepsilon_{12},T)$ by straining the B2 and B19' supercells. Next, under QHA, we calculated the temperature-dependent elastic constants of B2 and B19', C^{B2}_{ijkl} and $C^{\mathrm{B19'}}_{ijkl}$. For B2,

$$\begin{aligned} C^{\mathrm{B2}}_{1111} = C^{\mathrm{B2}}_{2222} &= \frac{1}{V_0^{\mathrm{B2}}}\frac{\partial^2 F}{\partial \eta_1^2}, \\ C^{\mathrm{B2}}_{1122} &= \frac{1}{2V_0^{\mathrm{B2}}}\left(\frac{\partial^2 F}{\partial \eta_2^2} - 2\frac{\partial^2 F}{\partial \eta_1^2}\right), \\ C^{\mathrm{B2}}_{2323} = C^{\mathrm{B2}}_{3131} &= \frac{1}{V_0^{\mathrm{B2}}}\frac{\partial^2 F}{\partial \eta_3^2}, \end{aligned} \tag{2}$$

where V_0^{B2} is the unstrained volume of the unit cell of B2. Other nonzero elastic constants for B2, $C^{\mathrm{B2}}_{3333}, C^{\mathrm{B2}}_{1133}(= C^{\mathrm{B2}}_{2233})$ and C^{B2}_{1212} can be derived using

the above equations. For B19',

$$
\begin{aligned}
C_{1111}^{\mathrm{B19'}} &= \frac{1}{V_0^{\mathrm{B19'}}}\frac{\partial^2 F}{\partial \eta_1^2}, \\
C_{2222}^{\mathrm{B19'}} &= \frac{1}{V_0^{\mathrm{B19'}}}\frac{\partial^2 F}{\partial \eta_2^2}, \\
C_{3333}^{\mathrm{B19'}} &= \frac{1}{V_0^{\mathrm{B19'}}}\frac{\partial^2 F}{\partial \eta_3^2}, \\
C_{1122}^{\mathrm{B19'}} &= \frac{1}{2V_0^{\mathrm{B19'}}}\left(\frac{\partial^2 F}{\partial \eta_4^2} - \frac{\partial^2 F}{\partial \eta_1^2} - \frac{\partial^2 F}{\partial \eta_2^2}\right), \\
C_{1133}^{\mathrm{B19'}} &= \frac{1}{2V_0^{\mathrm{B19'}}}\left(\frac{\partial^2 F}{\partial \eta_5^2} - \frac{\partial^2 F}{\partial \eta_1^2} - \frac{\partial^2 F}{\partial \eta_3^2}\right), \\
C_{2233}^{\mathrm{B19'}} &= \frac{1}{2V_0^{\mathrm{B19'}}}\left(\frac{\partial^2 F}{\partial \eta_6^2} - \frac{\partial^2 F}{\partial \eta_2^2} - \frac{\partial^2 F}{\partial \eta_3^2}\right), \\
C_{2323}^{\mathrm{B19'}} &= \frac{1}{V_0^{\mathrm{B19'}}}\frac{\partial^2 F}{\partial \eta_7^2}, \\
C_{2323}^{\mathrm{B19'}} &= \frac{1}{V_0^{\mathrm{B19'}}}\frac{\partial^2 F}{\partial \eta_8^2}, \\
C_{1212}^{\mathrm{B19'}} &= \frac{1}{V_0^{\mathrm{B19'}}}\frac{\partial^2 F}{\partial \eta_9^2}, \\
C_{2223}^{\mathrm{B19'}} &= \frac{1}{2V_0^{\mathrm{B19'}}}\left(\frac{\partial^2 F}{\partial \eta_{10}^2} - \frac{\partial^2 F}{\partial \eta_2^2} - \frac{\partial^2 F}{\partial \eta_7^2}\right), \qquad (3)
\end{aligned}
$$

where $V_0^{\mathrm{B19'}}$ is the unstrained volume of the unit cell of B19'. The strains $\eta_i (i = 1, 2, 3, \dots)$ used for these calculations are listed in Table 1 [29, 30]. Due to tensor symmetry, $C_{ijkl} = C_{jikl} = C_{ijlk} = C_{klij}$ and the rest of the elastic constants not mentioned here were assumed to be zero. It must be mentioned that we have included $C_{2223}^{\mathrm{B19'}}$ of the B19' structure in our calculations because previous studies have reported that it has a non-negligibly large value [23, 26, 31, 32].

For DFT calculations, we used the Vienna Ab initio Simulation Package [33]. The electron-ion interaction in DFT was described using the projector-augmented wave method [34] and the exchange correlation between electrons was treated using the Perdew–Burke–Ernzerhof generalized gradient approximation [35]. An energy cutoff of 500 eV was used for the plane-wave expansion. A $7 \times 7 \times 15$ k-point mesh was used for the B2 and B19 structures. The

energy convergence criteria for the electronic and ionic structure relaxation were set to 10^{-8} and 10^{-4} eV, respectively. Spin polarization was not considered in the present study. For the phonon calculation, Phonopy software was employed [36], ρ was obtained using the force constants, which were calculated using DFPT. A $10 \times 10 \times 20$ q-point mesh was used for both B2 and B19' structures. The value of η (provided as listed in Table 1) was varied from -0.03 to 0.03 with a step size of 0.005, and the obtained values of F was interpolated using a quadratic function to calculate the second derivatives required in equations (2) and (3).

Table 1: Strain forms used for phonon calculation under QHA for B2 and B19' structures.

	ε_{11}	ε_{22}	ε_{33}	ε_{23}	ε_{31}	ε_{12}
B2						
η_1	η	0	0	0	0	0
η_2	η	η	0	0	0	0
η_3	0	0	0	η	0	0
B19'						
η_1	η	0	0	0	0	0
η_2	0	η	0	0	0	0
η_3	0	0	η	0	0	0
η_4	η	η	0	0	0	0
η_5	η	0	η	0	0	0
η_6	0	η	η	0	0	0
η_7	0	0	0	η	0	0
η_8	0	0	0	0	η	0
η_9	0	0	0	0	0	η
η_{10}	0	η	0	η	0	0

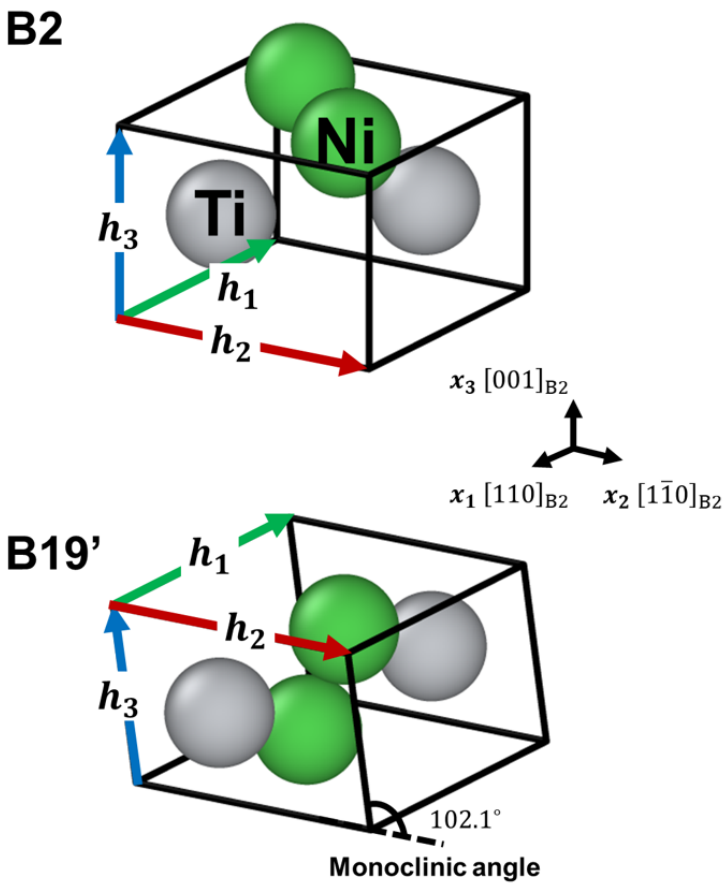

Figure 1: Atomic structures of B2 matrix and B19' secondary phase. Both the structures contain two Ti and two Ni atoms. The supercells used for the DFT calculation are shown by black lines and the edge vectors ($\boldsymbol{h_1}$, $\boldsymbol{h_2}$, and $\boldsymbol{h_3}$) are shown as red, green, and blue arrows, respectively. The monoclinic angle of the B19' structure is also shown. The atomic structures were visualized using OVITO software [37].

2.2. Results

The calculated η_i $(i = 1, 2, 3)$ vs. free energy plots at different temperatures are shown in Fig. 2. (Because of the large amount of data, we only show the results for η_1, η_2 and η_3.) Using the second derivative of the fitting quadratic curve, temperature-dependent elastic constants were calculated, and the results are shown in Fig. 3. The values of $\tilde{C}^{\mathrm{B2}}_{1111}$, $\tilde{C}^{\mathrm{B2}}_{1122}$, and $\tilde{C}^{\mathrm{B2}}_{2323}$ in the conventional $[100]_{\mathrm{B2}} - [010]_{\mathrm{B2}} - [001]_{\mathrm{B2}}$ coordinate system at 0 K for B2 case were 180, 152 and 50 GPa, respectively, which are consistent with those reported in previous DFT calculations [8, 38]. Moreover, the corresponding values at 300 K were 200, 152 and 71 GPa, respectively, which are similar to previous experimental results of near-equiatomic TiNi alloys (150 to 200, 100 to 150, and 30 to 35 GPa, respectively; the large deviation in the value of $\tilde{C}^{\mathrm{B2}}_{1122}$ is acknowledged) [25]. The trends that $\tilde{C}^{\mathrm{B2}}_{1111}$ and $\tilde{C}^{\mathrm{B2}}_{2323}$ increase with an increase in temperature and $\tilde{C}^{\mathrm{B2}}_{1122}$ is almost independent of temperature are also consistent with previous experimental observations [25]. The observed elastic constants of the B19' structure at 0 K also more or less agree with previous DFT studies [26, 31, 32], and their temperature dependence was not as significant as that of B2. This suggests that the shape memory effect, which is the instability of the heterogeneous B19' phase at high temperatures, is due to larger differences between the elastic constants of the B2 and B19' structures. Similar suggestions that elastic softening causes B2 to B19' phase transformation have also been made from experimental observations [4, 24].

The temperature-dependent eigenstrains were also calculated using phonon analysis under QHA. The shift in the critical point of the fitting quadratic curves in Fig. 2 gives the thermal strain [39]; this is shown in Fig. 4. The gradient of the fitting linear line of the plot along a given direction gives the coefficient of thermal expansion along that direction, and the calculated values are 1.12×10^{-5} for B2 and 2.68×10^{-5}, 1.65×10^{-5}, and 1.62×10^{-5} 1/K for the B19' structure along $[110]_{\mathrm{B2}}$, $[1\bar{1}0]_{\mathrm{B2}}$, and $[001]_{\mathrm{B2}}$ directions, respectively. Using these coefficients, we derived the temperature-dependent lattice constants and the edge vectors $\boldsymbol{h_1}(T)$, $\boldsymbol{h_2}(T)$, and $\boldsymbol{h_3}(T)$ (see Fig. 1 for reference) of the B2 and B19' structures. These were then used to define the supercell matrix $\boldsymbol{H}(T)$, i.e., $\boldsymbol{H} \equiv [\boldsymbol{h_1}\ \boldsymbol{h_2}\ \boldsymbol{h_3}]$, for each structure. Using the supercell matrices of the B2 and B19' structures ($\boldsymbol{H_{B2}}(T)$ and $\boldsymbol{H_{B19'}}(T)$, respectively), the eigenstrain of the B19' phase ($\epsilon_{ij}^{\mathrm{B19'}}$) was computed in the

form of a Green strain as

$$\epsilon_{ij}^{\mathrm{B19'}}(T) = \frac{1}{2}\left(\boldsymbol{J}^{\mathbf{T}}\boldsymbol{J} - \boldsymbol{I}\right), \tag{4}$$

where $\boldsymbol{J}^{\mathbf{T}} = \boldsymbol{H}_{\boldsymbol{B19'}}\left(\boldsymbol{H}_{\mathbf{B2}}\right)^{-1}$ denotes the deformation tensor [22]. The calculated temperature-dependent eigenstrains are shown in Fig. 5. Herein, it can be observed that the normal components of the eigenstrain increases with an increase in temperature, which is due to different thermal expansions of the B2 and B19' structures. However, the increment is of the order of 10^{-3} between 0 and 500 K, indicating that the effect of thermal expansion is not significant.

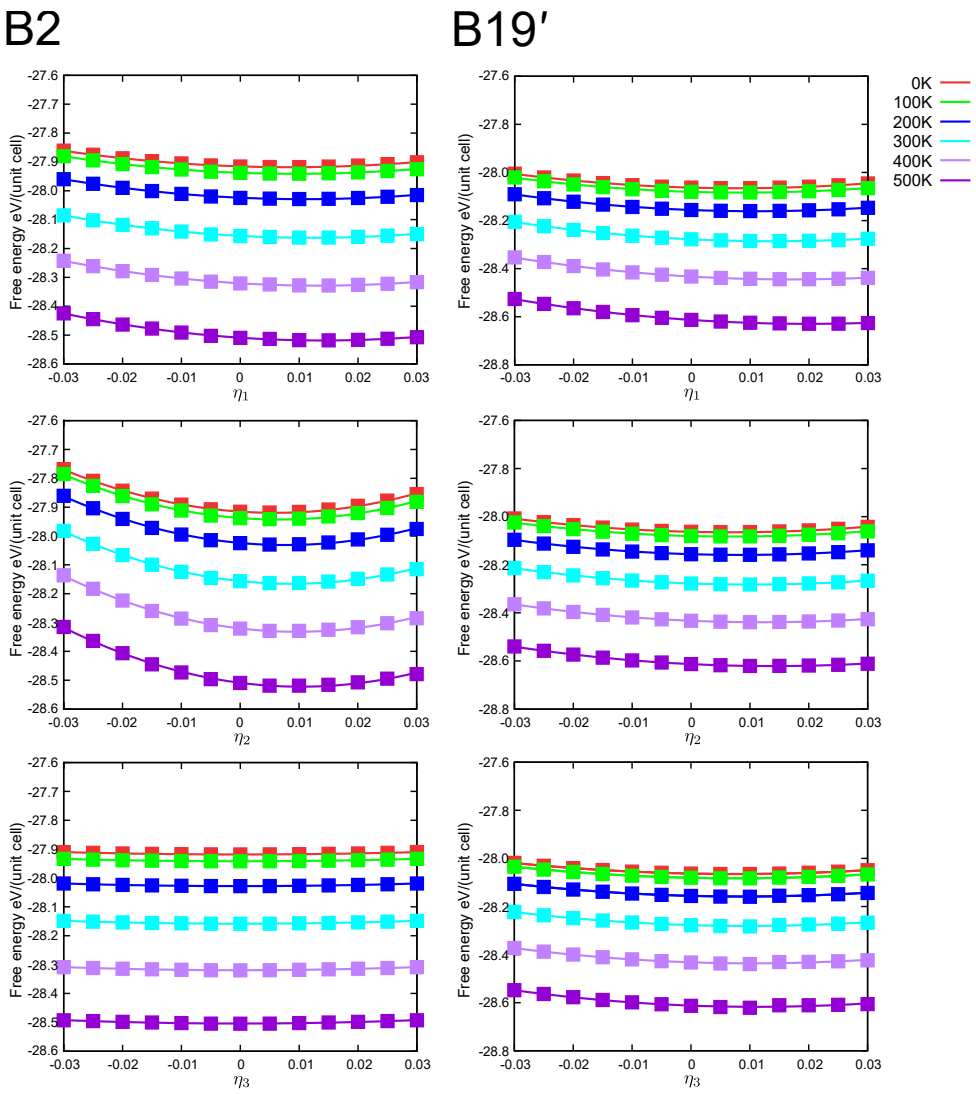

Figure 2: Result of phonon analysis under QHA: η_i $(i = 1, 2, 3 \dots)$ vs free energy plots for B2 and B19' atomic structures at 0, 100, 200, 300, 400 and 500 K. Note only η_1, η_2 and η_3 cases are shown representatively for B19' structure. The curves are fitted quadratic functions.

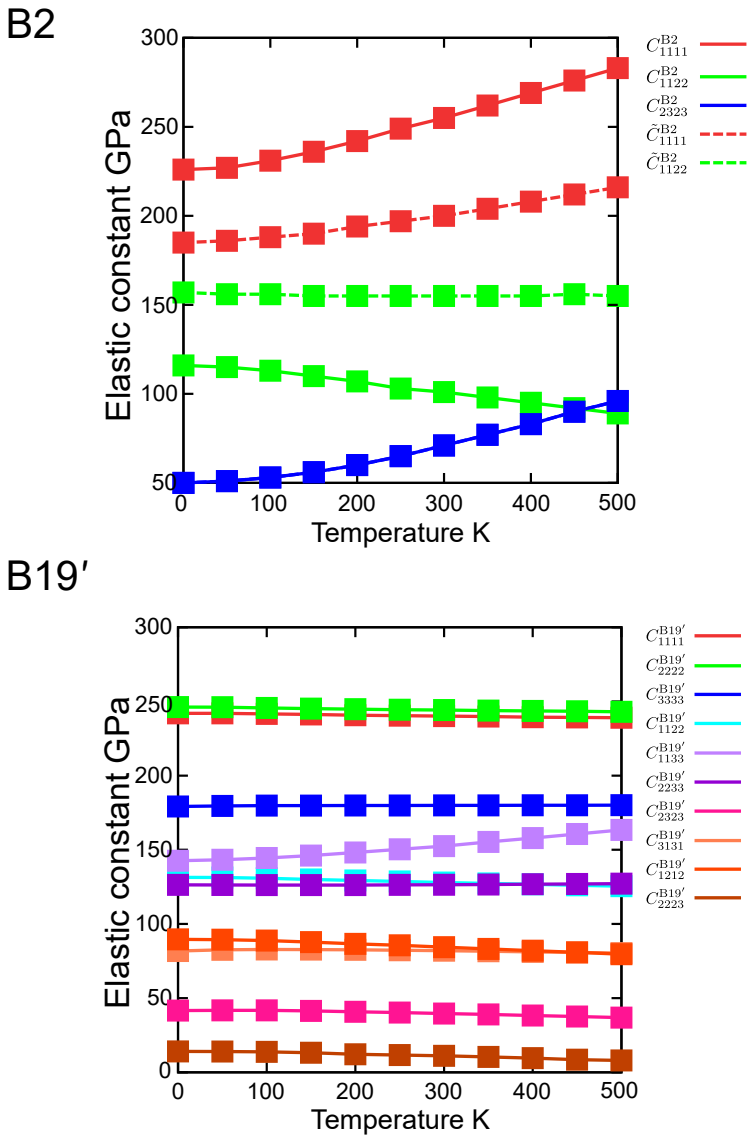

Figure 3: Temperature vs. elastic constant plots for the B2 and B19' atomic structures. The elastic constants were generally defined in the $[110]_{\mathrm{B2}} - [1\bar{1}0]_{\mathrm{B2}} - [001]_{\mathrm{B2}}$ coordinate system in this study. For the B2 structure, the elastic constants defined in the conventional $[100]_{\mathrm{B2}} - [010]_{\mathrm{B2}} - [001]_{\mathrm{B2}}$ coordinate system, $\tilde{C}^{\mathrm{B2}}_{1111} (= \tilde{C}^{\mathrm{B2}}_{2222} = \tilde{C}^{\mathrm{B2}}_{3333})$ and $\tilde{C}^{\mathrm{B2}}_{1122} (= \tilde{C}^{\mathrm{B2}}_{1133} = \tilde{C}^{\mathrm{B2}}_{2233})$, are also shown for reference. Note $\tilde{C}^{\mathrm{B2}}_{2323} (= \tilde{C}^{\mathrm{B2}}_{3131} = \tilde{C}^{\mathrm{B2}}_{1212}) = C^{\mathrm{B2}}_{2323}$.

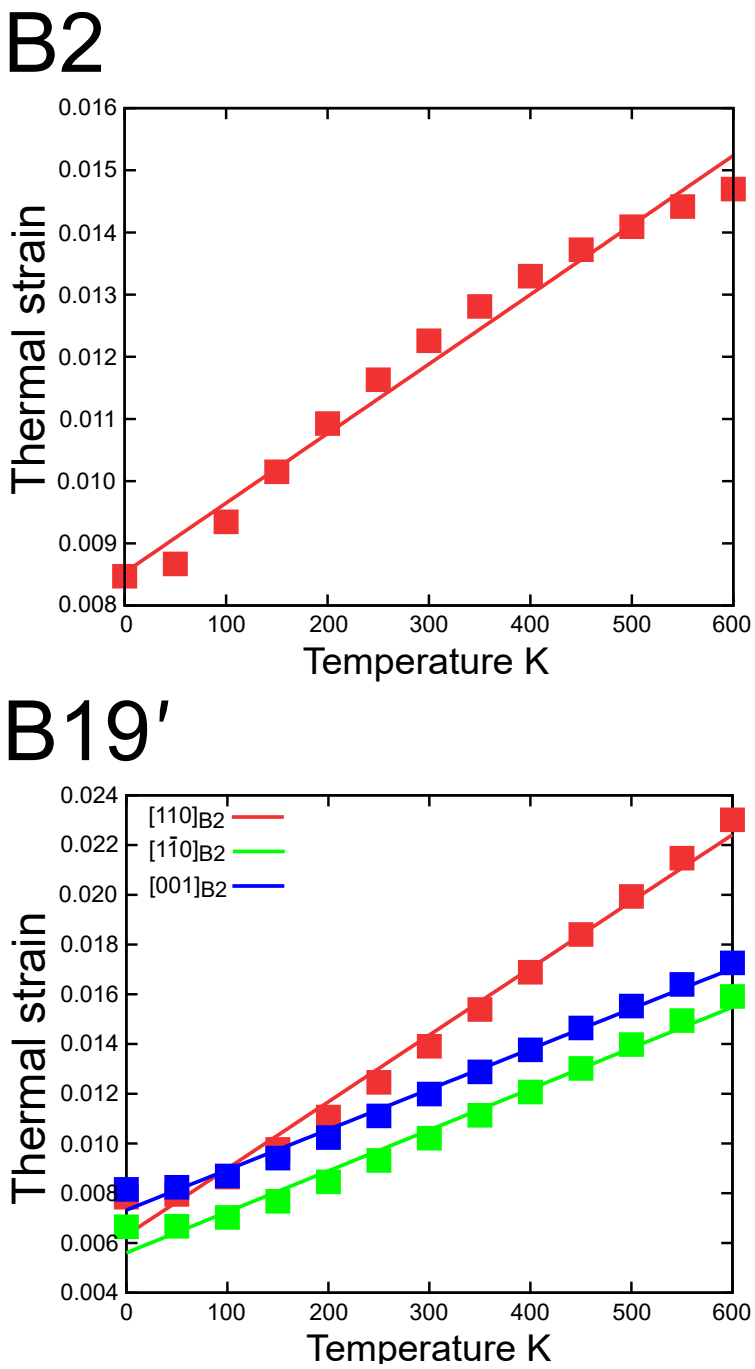

Figure 4: Temperature vs. thermal strain plots for the B2 and B19' atomic structures.

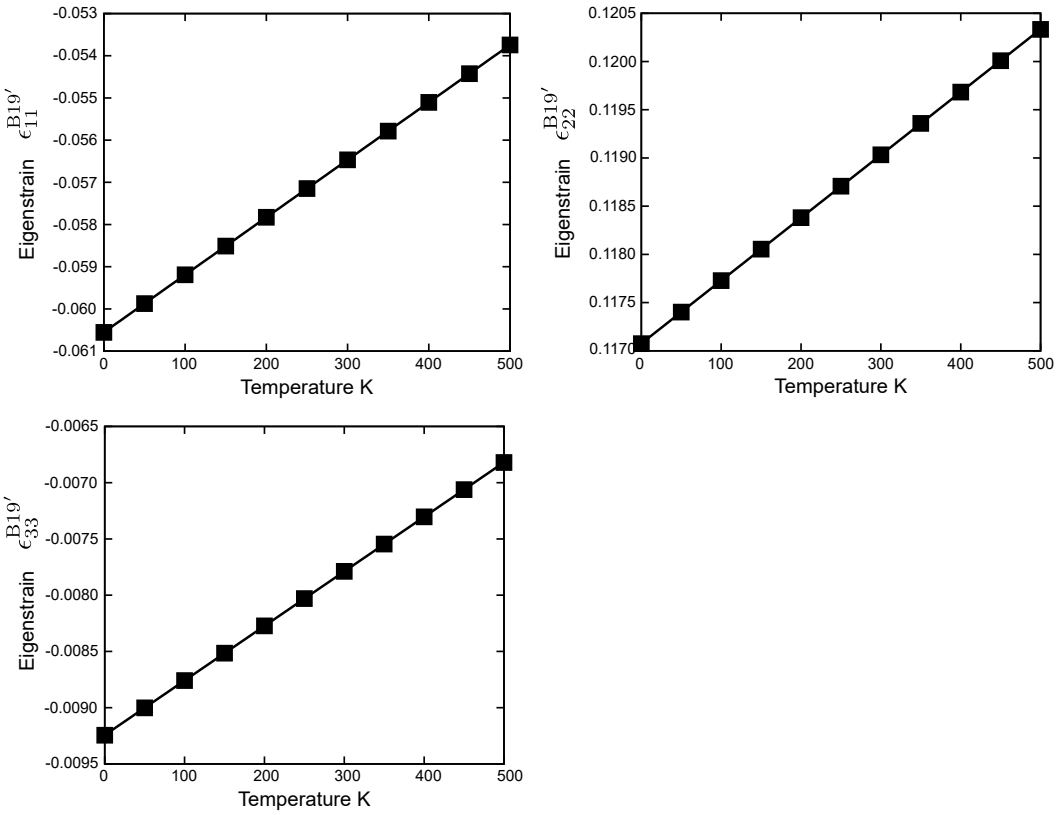

Figure 5: Temperature vs. $\epsilon_{11}^{\mathrm{B19}'}$, $\epsilon_{22}^{\mathrm{B19}'}$, and $\epsilon_{33}^{\mathrm{B19}'}$ plots. The eigenstrain $\epsilon_{23}^{\mathrm{B19}'} = 0.116$ was observed to be independent of temperature. Note that $\epsilon_{ij}^{\mathrm{B19}'} = \epsilon_{ji}^{\mathrm{B19}'}$ and the values of other $\epsilon_{ij}^{\mathrm{B19}'}$ are zero.

3. Eshelby's ellipsoidal inclusion analysis

3.1. Methodology

The heterogeneously nucleated B19' phase in the B2 matrix was elastically deformed from its original strain-free shape. In micromechanics, this elastically deformed shape is described as the total strain (the original zero-strain shape is defined as the shape of the matrix), whereas the eigenstrain describes the original shape of the secondary phase [21]. We predicted the morphology and total strains of the B19' phase by considering the B19' phase in the B2 matrix as an ellipsoidal inclusion [40, 41]. The ellipsoid was defined as $\frac{x_1^2}{a_1^2} + \frac{x_2^2}{a_2^2} + \frac{x_3^2}{a_3^2} = 1$, where a_i is the half-axis of the ellipsoid along the three orthogonal directions. Considering that previous studies have suggested that the B19' phase in the B2 matrix of TiNi alloys are disk-shaped [23, 42–44], we simply used $(a_1; a_2; a_3) = (10/\sqrt{2}; 10/\sqrt{2}; 1)$. Then, the stable orientation of the B19' phase with the minimum elastic energy increment ΔE in the B2 matrix was evaluated, and its total strains for this orientation were calculated. Note that, although a V-shaped B19' phase was also experimentally observed [5], we did not consider such a shape owing to the limitation of Eshelby's ellipsoidal inclusion. Additionally, we did not include the interfacial energy term between the B2 and B19' structures in this study. As the size of the B19' phase in the B2 matrix is usually on the millimeter or micrometer scale [4], we believe that the volume-dependent elastic energy is dominant and the area-dependent interfacial energy is not significant for the transformation.

For Eshelby's ellipsoidal inclusion, generally, the total strain $\hat{\varepsilon}_{ij}$ is described by the eigenstrain ϵ_{mn} using the Einstein summation convention [21] as:

$$\hat{\varepsilon}_{kl} = S_{klmn}\epsilon_{mn}, \tag{5}$$

where S_{klmn} denotes the Eshelby tensor [40]. In this study, considering the elastic anisotropy of the B2 structure [21, 45], S_{klmn} is expressed as follows:

$$S_{klmn} = \frac{1}{8\pi} C^{\mathrm{B2}}_{pqmn} \int_{-1}^{1} d\zeta_3 \int_{0}^{2\pi} \left(\frac{\xi_l \xi_q N_{kp}(\xi_1, \xi_2, \xi_3) + \xi_k \xi_q N_{lp}(\xi_1, \xi_2, \xi_3)}{D(\xi_1, \xi_2, \xi_3)} \right) d\theta, \tag{6}$$

where

$$D(\xi_1, \xi_2, \xi_3) \;=\; P_{pqr}(C^{\mathrm{B2}}_{pj1l}\xi_j\xi_l)(C^{\mathrm{B2}}_{qm2n}\xi_m\xi_n)(C^{\mathrm{B2}}_{rs3t}\xi_s\xi_t),$$

and

$$N_{km}(\xi_1, \xi_2, \xi_3) \;=\; \frac{1}{2} P_{kst} P_{mnr} (C^{\mathrm{B2}}_{sjnl} \xi_l \xi_j)(C^{\mathrm{B2}}_{turv} \xi_u \xi_v),$$

correspond to the determinant and cofactor of $K_{km} = C^{\mathrm{B2}}_{klmn} \xi_l \xi_n$, respectively. P_{pqr} denotes the permutation tensor. By using ζ_3 and θ, $[\xi_1; \xi_2; \xi_3]$ can be described as

$$\begin{bmatrix} \xi_1 \\ \xi_2 \\ \xi_3 \end{bmatrix} = \begin{bmatrix} \frac{\sqrt{1-\zeta_3^2}\cos\theta}{a_1} \\ \frac{\sqrt{1-\zeta_3^2}\sin\theta}{a_2} \\ \frac{\zeta_3}{a_3} \end{bmatrix}.$$

The differences between the elastic constants of the B2 matrix and the B19' phase can be considered using Eshelby's equivalent inclusion theory [21, 41]. Fictitious strain $\tilde{\epsilon}_{ij}$ was calculated using the following equation:

$$C^{\mathrm{B19'}}_{ijkl}(S_{klmn}\tilde{\epsilon}_{mn} - \epsilon^{\mathrm{B19'}}_{kl}) = C^{\mathrm{B2}}_{ijkl}(S_{klmn}\tilde{\epsilon}_{mn} - \tilde{\epsilon}_{kl}). \tag{7}$$

Next, the total strain of the B19' phase was calculated as $\hat{\varepsilon}^{\mathrm{B19'}}_{kl} = S_{klmn}\tilde{\epsilon}_{mn}$ using Equation (5). Using $\hat{\varepsilon}^{\mathrm{B19'}}_{kl}$, the internal stress of the B19' phase, σ_{ij}, was calculated as

$$\sigma_{ij} = C^{\mathrm{B2}}_{ijkl}(\hat{\varepsilon}^{\mathrm{B19'}}_{kl} - \tilde{\epsilon}_{kl}). \tag{8}$$

Using these values, the elastic energy increment ΔE due to the existence of the B19' phase in the B2 matrix was described as

$$\Delta E = -\frac{1}{2}\sigma_{ij}\epsilon^{\mathrm{B19'}}_{ij}. \tag{9}$$

The change in the orientation of the B19' phase was considered by changing the coordinate system of the eigenstrains and elastic constants from the original $\boldsymbol{x_1} - \boldsymbol{x_2} - \boldsymbol{x_3}$ to $\boldsymbol{x'_1} - \boldsymbol{x'_2} - \boldsymbol{x'_3}$ using the following rotation matrix [22, 46]:

$$R_{ij} \;=\; \begin{bmatrix} \cos\psi\cos\phi & \cos\psi\sin\phi & -\sin\psi \\ -\sin\phi & \cos\phi & 0 \\ \sin\psi\cos\phi & \sin\psi\sin\phi & \cos\psi \end{bmatrix}. \tag{10}$$

In our model, the $\boldsymbol{x'_3}$ axis was perpendicular to the disk. By varying the angles ϕ ($0° < \phi < 180°$) and ψ ($0° < \psi < 180°$), we detected the orientation

with the minimum of ΔE as the stable morphology of the B19' phase and calculated its total strains $\hat{\varepsilon}_{ij}^{\mathrm{B19'}}$ for each temperature using the temperature-dependent elastic constants and eigenstrains calculated earlier (see Figs. 3 and 5, respectively). For further details of our atomistically informed Eshebly's ellipsoidal inclusion analysis and its fundamental physics, the reader is referred to our previous studies and Mura's micromechanics textbook [21–23].

3.2. Result

Figure 6 shows the ΔE maps as functions of ϕ and ψ at 300 K. The $\Delta E(\phi, \psi)$ distribution is similar to that in our previous study without the phonon effect [23]; ΔE was low in the region ($60^\circ < \phi < 120^\circ, 140^\circ < \psi < 160^\circ$) and the minimum of ΔE was at $(90^\circ, 150^\circ)$: $\Delta E = 0.52$ GJ/m^3. We confirmed that the $\Delta E(\phi, \psi)$ distribution is not sensitive to temperature, and the region with low or minimum ΔE does not vary with temperature. Note that assuming the experimental habit plane as the disk plane in this study, the habit plane of the B19' phase, $(249)_{\mathrm{B2}}$ [5, 44] approximately corresponded to the disk with an angle $(\phi, \psi) = (80^\circ, 150^\circ)$, which is consistent with our results.

The temperature vs. total strain of $(\phi, \psi) = (90^\circ, 150^\circ)$ disk plots are shown in Fig. 7. Owing to the back stress from the B2 matrix, the total strains were generally smaller than the eigenstrains, but, similar to the eigenstrains, they increased with an increase in temperature. On the other hand, we believe that the decrease in $\hat{\varepsilon}_{22}^{\mathrm{B19'}}$ and $\hat{\varepsilon}_{23}^{\mathrm{B19'}}$ components with an increase in temperature and the larger magnitude of $\hat{\varepsilon}_{33}^{\mathrm{B19'}}$ than $\epsilon_{33}^{\mathrm{B19'}}$ are due to the increased dissimilarity of the elastic constants of the B2 and B19' structures. In fact, the decrease in $\hat{\varepsilon}_{33}^{\mathrm{B19'}}$ is consistent with the experimentally observed thermal shrinkage of the B19' phase along the $\boldsymbol{c}$ ($[1\bar{1}0]_{\mathrm{B2}}$) direction [3].

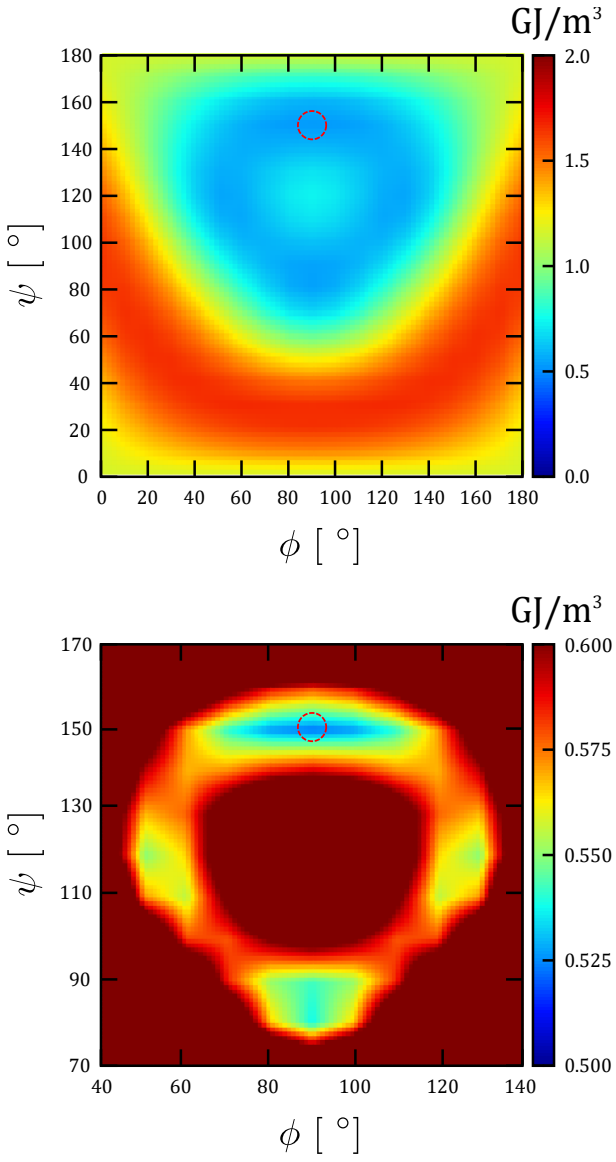

Figure 6: Elastic energy increment ΔE variation with respect to ϕ and ψ. The bottom figure is an enlarged view of the region bounded by $(40^\circ < \phi < 140^\circ, 70^\circ < \psi < 170^\circ)$. Broken circles indicate the area with minimum ΔE.

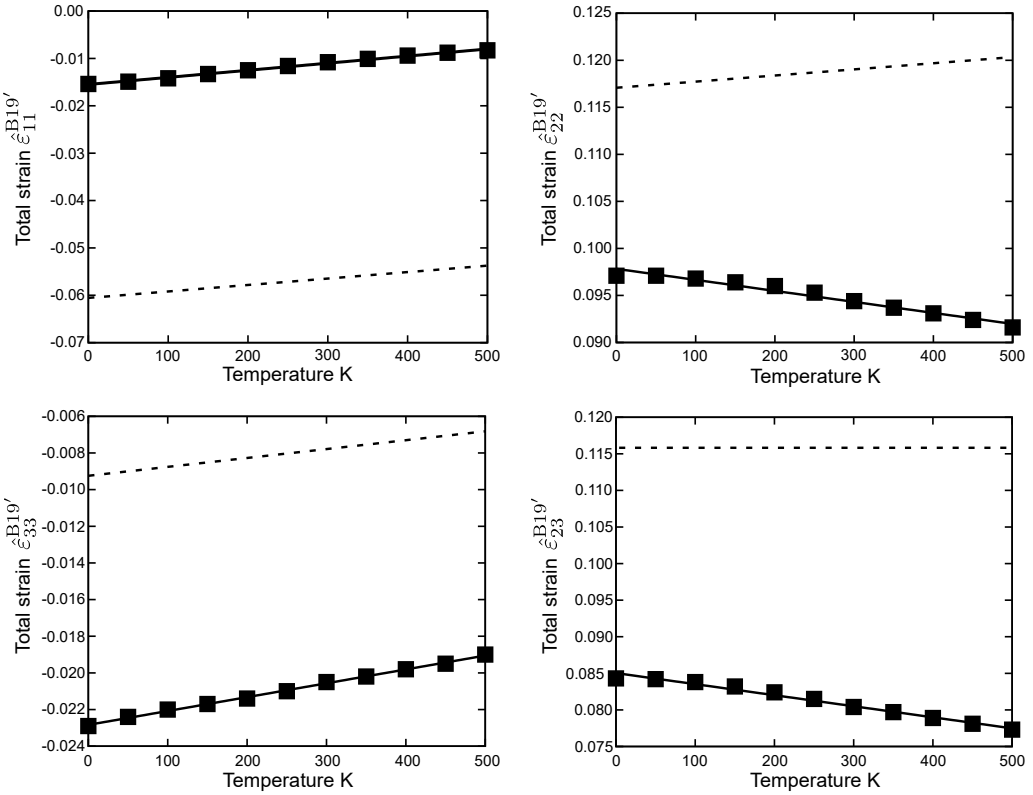

Figure 7: Temperature vs. total strain plots for $\hat{\varepsilon}_{11}^{\mathrm{B19'}}$, $\hat{\varepsilon}_{22}^{\mathrm{B19'}}$, $\hat{\varepsilon}_{33}^{\mathrm{B19'}}$ and $\hat{\varepsilon}_{23}^{\mathrm{B19'}}$ components. Temperature vs eigenstrains lines (in Fig. 5) for each component are also shown as dashed lines for comparison. The values of other $\hat{\varepsilon}_{ij}^{\mathrm{B19'}}$ are zero. The total strains are those of the disk with minimum ΔE.

4. Temperature-dependent stability of heterogeneous B19' phase in B2 matrix

As has been mentioned previously, the heterogeneously nucleated B19' phase is elastically deformed in the B2 matrix, and its shape is described by the total strains shown in Fig. 7. To reproduce the atomic structure of the elastically deformed B19' phase, we changed the edge vectors of B19' supercell to a strained one using the calculated total strains, fixing the internal coordinates [47]. Then, the internal coordinates were relaxed without changing the edge vectors to reduce the residual forces. Considering this strained B19' atomic structure as an elastically deformed B19' in B2 matrix, we calculated its free energy using DFT calculations and phonon analysis. Comparing the free energy with that of the stable B2 structure for each temperature, which was obtained from the critical point of the strain vs. free energy curves shown in Fig. 2, temperature-dependent stability of heterogeneous nucleated B19' phase was predicted.

Figure 8 shows the structures of the elastically deformed B19' at 300 K and the strain-free B19'. Herein, it can be observed that the monoclinic angle shifted from 102.1° (strain-free) to 99.3° (elastically deformed), which is closer to the experimentally observed 97.8°, indicating that the modeled B19' phase in near-equiatomic TiNi alloys was closer to experimentally observed structure than that obtained using conventional DFT calculations [3]. The temperature vs. free energy plots for the elastically deformed B19' and B2 structures are shown in Fig. 9 (a). Herein, it can be observed that the free energy of B19' phase was lower than that of B2 at low temperatures and crossover occurred at 300 K. This agrees well with experimentally observed Ms temperature of the B19' phase [3–5, 19, 20]. To the best of our knowledge, this is the first successful theoretical prediction of the phase transformation temperature that tallies with experimental observations. Because the eigenstrains of the B19' structure were not sensitive to temperature (Fig. 5), we concluded that the dissimilarity in the elastic constants of the B19' phase and B2 matrix results in this crossover and, hence, the shape memory effect of near-equiatomic TiNi alloy. Although a similar suggestion has already been made from experimental observations [4, 24], this is the first study to confirm that using a theoretical approach. Even though the free energy difference between the B2 and the elastically deformed B19' structures may seem small (Fig. 9) (which is because of the small size of our simulation cell (angstrom-scale)), this difference in realistic systems (micro-scale) can

become as large as 10^9 to 10^{10} eV at 400 K.

Additionally, the variation of E^{ele} and E^{pho} with temperature are shown in Fig. 9 (b) and (c), respectively. From these figures, it can be concluded that the phase stability at low temperatures (0250 K) is dominated by the E^{ele} term, implying that the B19' phase is stable in such a scenario. At approximately 300 K, the E^{pho} term becomes significant and stabilizes B2 matrix owing to the decrease in the difference of E^{ele} between B2 and elastically deformed B19'. Beyond 300 K, E^{ele} of the B2 structure becomes lower than that of the elastically deformed B19' structure, and the difference in their E^{pho} values become negligible.

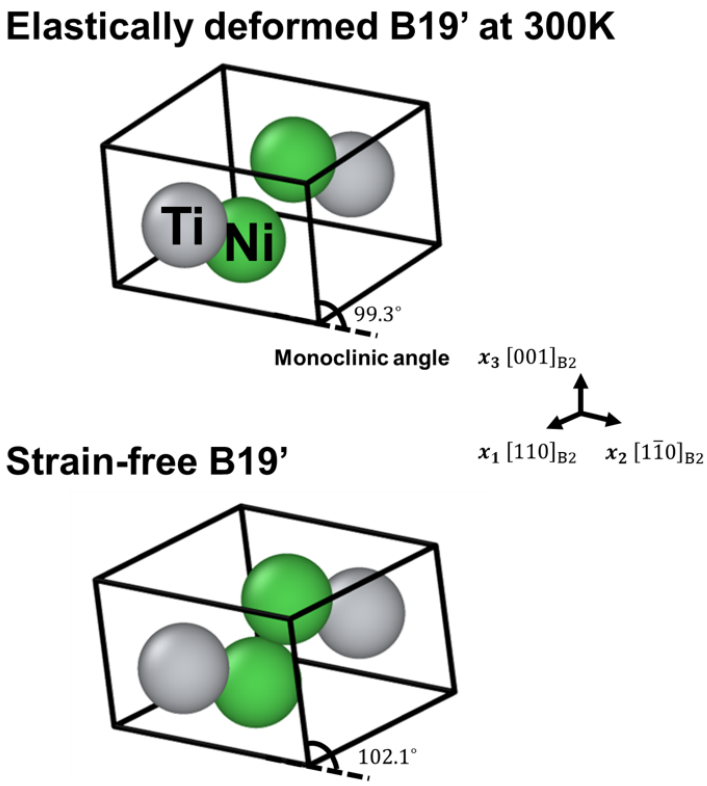

Figure 8: Atomic structures of elastically deformed B19' structure at 300 K. The original strain-free B19 structure (in Fig. 1) is also shown for the comparison.

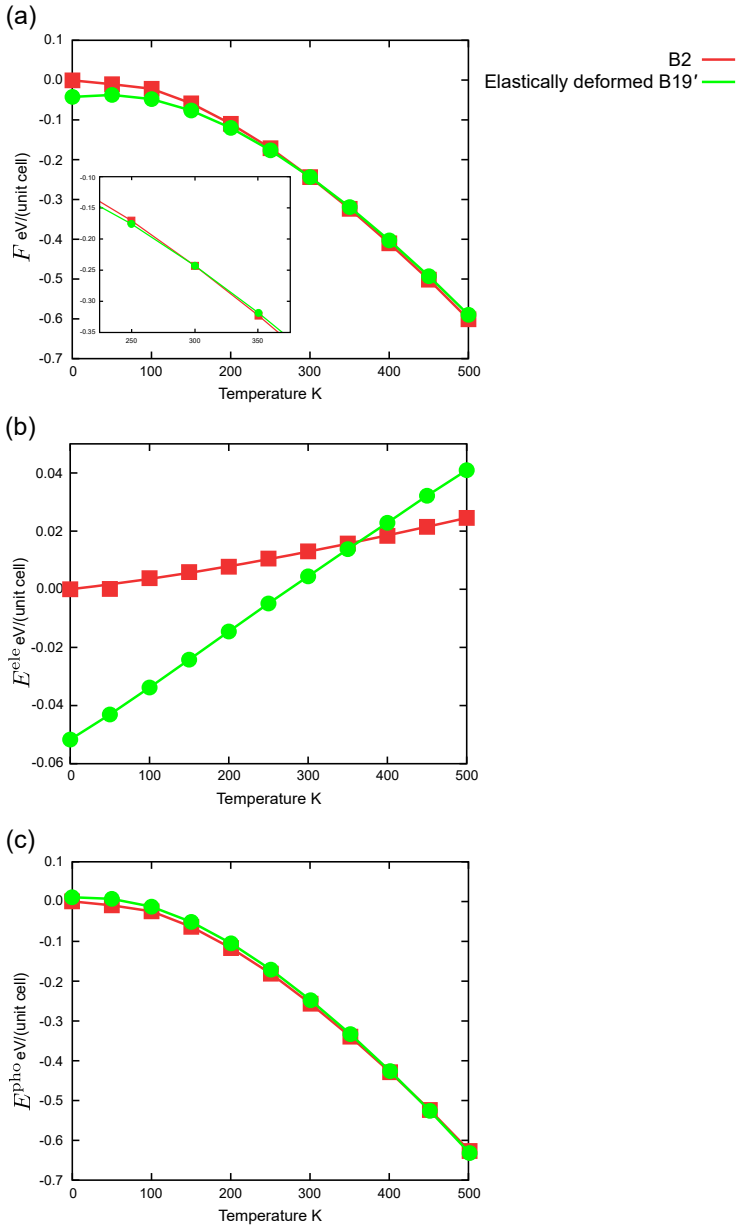

Figure 9: Temperature dependence of the free energies of B2 and elastically deformed B19' structures: temperature vs (a) free energy F, (b) E^{int}, and (c) E^{pho}. The energies are relative to that of the B2 structure at 0 K.

5. Summary

In this study, we energetically predicted the temperature-dependent stability of the heterogeneous B19' phase in B2 matrix for a near-equiatomic TiNi alloy using DFT and phonon analysis informed Eshelby's ellipsoidal inclusion. The temperature-dependent eigenstrains and elastic constants for Eshelby's ellipsoidal inclusion were calculated using DFT and phonon analyses under QHA. The stable orientation of the disk-shaped B19' phase in B2 matrix and its total strain were energetically evaluated with respect to temperature using Eshelby's ellipsoidal inclusion analysis. Using the total strains, the elastically deformed atomic structures of the heterogeneous B19' phase in B2 matrix were determined, and its temperature-dependent free energy was calculated using DFT and phonon analysis. Comparing the temperature-dependent free energy of elastically deformed B19' and B2 structures, we successfully predicted that the phase transformation from the heterogeneous B19' phase to B2 matrix occurs at 300 K, which is consistent with the experimental Ms temperature of the B19' phase. The temperature-dependent difference in the elastic constants between the B19' phase and B2 matrix promotes the phase transformation, which is the origin of the shape memory effect of near-equiatomic TiNi alloys.

Acknowledgements

This work was partially supported by the Japan Society for the Promotion of Science (JSPS [grant number 21K03771]. DFT simulations were partly performed using OCTOPUS large-scale computer systems at the Cybermedia Center, Osaka University.

References

[1] J. Mohd Jani, M. Leary, A. Subic, M. A. Gibson, A review of shape memory alloy research, applications and opportunities, Mater. Des. 56 (2014) 1078–1113.

[2] W. J. Buehler, J. V. Gilfrich, R. C. Wiley, Effect of low-temperature phase changes on the mechanical properties of alloys near composition TiNi, J. Appl. Phys. 34 (1963) 1475–1477.

[3] S. D. Prokoshkin, A. V. Korotitskiy, V. Brailovski, S. Turenne, I. Y. Khmelevskaya, I. B. Trubitsyna, On the lattice parameters of phases in binary Ti-Ni shape memory alloys, Acta Mater. 52 (2004) 4479–4492.

[4] K. Otsuka, X. Ren, Physical metallurgy of Ti-Ni-based shape memory alloys, Prog. Mater. Sci. 50 (5) (2005) 511–678.

[5] M. Nishida, T. Nishiura, H. Kawano, T. Inamura, Self-accommodation of B19' martensite in Ti-Ni shape memory alloys-Part I. Morphological and crystallographic studies of the variant selection rule, Phil. Mag. 92 (2012) 2215–2233.

[6] A. S. K. Mohammed, H. Sehitoglu, Modeling the interface structure of type II twin boundary in B19' NiTi from an atomistic and topological standpoint, Acta Mater. 183 (2020) 93–109.

[7] X. Huang, G. J. Ackland, K. M. Rabe, Crystal structures and shape-memory behaviour of NiTi, Nature Mater. 2 (2003) 307–311.

[8] N. Hatcher, O. Y. Kontsevoi, A. J. Freeman, Martensitic transformation path of NiTi, Phys. Rev. B 79 (2009) 020202.

[9] K. Guda Vishnu, A. Strachan, Phase stability and transformations in NiTi from density functional theory calculations, Acta Mater. 58 (2010) 745–752.

[10] W. S. Ko, B. Grabowski, J. Neugebauer, Development and application of a Ni-Ti interatomic potential with high predictive accuracy of the martensitic phase transition, Phys. Rev. B 92 (2015) 134107.

[11] J. B. Haskins, A. E. Thompson, J. W. Lawson, Ab initio simulations of phase stability and martensitic transitions in NiTi, Phys. Rev. B 94 (2016) 214110.

[12] W. S. Ko, S. B. Maisel, B. Grabowski, J. B. Jeon, J. Neugebauer, Atomic scale processes of phase transformations in nanocrystalline NiTi shape-memory alloys, Acta Mater. 123 (2017) 90–101.

[13] W. S. Ko, Temperature dependence of NiTi martensite structures: Density functional theory calculations, Scripta Mater. 154 (2018) 134–138.

[14] P. Kumar, U. V. Waghmare, First-principles phonon-based model and theory of martensitic phase transformation in NiTi shape memory alloy, Materialia 9 (2020) 100602.

[15] J. B. Haskins, H. Malmir, S. J. Honrao, L. A. Sandoval, J. W. Lawson, Low-temperature mechanical instabilities govern high-temperature thermodynamics in the austenite phase of shape memory alloy constituents: ab initio simulations of NiTi, NiZr, NiHf, PdTi, and PtTi, Acta Mater. 212 (2021) 116872.

[16] W. S. Choi, E. L. Pang, W. S. Ko, H. Jun, H. J. Bong, C. Kirchlechner, D. Raabe, P. P. Choi, Orientation-dependent plastic deformation mechanisms and competition with stress-induced phase transformation in microscale NiTi, Acta Mater. 208 (2021) 116731.

[17] C. Lv, G. Wang, X. Zhang, B. Luo, N. Luo, H. Song, F. Wu, H. Wu, F. Tan, J. Zhao, C. Liu, C. Sun, New explanation for the existence of B19' phase in NiTi alloy from the perspective of twinning martensite, Scr. Mater. 214 (2022) 114644.

[18] X. Tao, Y. Yang, H. Zong, X. Ding, K. Yu, T. Lookman, J. Sun, Molecular dynamics simulations of ultralow hysteretic behavior in super-elastic shape memory alloys, Acta Mater. 232 (2022) 117973.

[19] T. H. Nam, T. Saburi, Y. Nakata, K. Shimizu, Shape memory characteristics and lattice deformation in Ti-Ni-Cu alloys, Mater. Trans. 31 (1990) 1050–1056.

[20] J. Khalil-Allafi, B. Amin-Ahmadi, The effect of chemical composition on enthalpy and entropy changes of martensitic transformations in binary NiTi shape memory alloys, J. Alloys Comp. 487 (2009) 363–366.

[21] T. Mura, Micromechanics of defects in solids, Martinus Nijhoff Publishers, Boston, 1987.

[22] A. Ishii, *Ab* initio morphology prediction of Zr hydride precipitates using atomistically informed Eshelby's ellipsoidal inclusion, Comput. Mater. Sci. 211 (2022) 111500.

[23] A. Ishii, Elastic investigation for the existence of B33 phase in TiNi shape memory alloys using atomistically informed Eshelby's ellipsoidal inclusion, Comput. Mater. Sci. 218 (2023) 111954.

[24] X. Ren, K. Otsuka, The role of softening in elastic constant c_{44} in martensitic transformation, Scripta Mater. 38 (1998) 1669–1675.

[25] X. Ren, N. Miura, J. Zhang, K. Otsuka, K. Tanaka, M. Koiwa, T. Suzuki, Y. I. Chumlyakov, M. Asai, A comparative study of elastic constants of Ti-Ni based alloys prior to martensitic transformation, Mater. Sci. Eng. A 312 (2001) 196–206.

[26] J. Wang, H. Sehitoglu, Martensite modulus dilemma in monoclinic NiTi-theory and experiments, Inter. J. Plast. 61 (2014) 17–31.

[27] D. Holec, M. Friák, A. Dlouhý, J. Neugebauer, Ab initio study of pressure stabilized NiTi allotropes: Pressure-induced transformations and hysteresis loops, Phys. Rev. B 84 (2011) 224119.

[28] X. Wu, D. Vanderbilt, D. R. Hamann, Systematic treatment of displacements, strains, and electric fields in density-functional perturbation theory, Phys. Rev. B 72 (2005) 035105.

[29] R. Golesorkhtabar, P. Pavone, J. Spitaler, P. Puschnig, C. Draxl, ElaStic: A tool for calculating second-order elastic constants from first principles, Comput. Phys. Comm. 184 (2013) 1861–1873.

[30] U. Argaman, G. Makov, First-principles study of the temperature dependence of the elastic constants of hcp titanium, Comput. Mater. Sci. 184 (2020) 109917.

[31] M. F. Wagner, W. Windl, Lattice stability, elastic constants and macroscopic moduli of NiTi martensites from first principles, Acta Mater. 56 (2008) 6232–6245.

[32] N. Hatcher, O. Y. Kontsevoi, A. J. Freeman, Role of elastic and shear stabilities in the martensitic transformation path of NiTi, Phys. Rev. B 80 (2009) 1–18.

[33] G. Kresse, J. Furthmüller, Efficient iterative schemes for ab initio total-energy calculations using a plane-wave basis set., Phys. Rev. B 54 (1996) 11169–11186.

[34] G. Kresse, D. Joubert, From ultrasoft pseudopotentials to the projector augmented-wave method, Phys. Rev. B 59 (1999) 1758–1775.

[35] J. Perdew, K. Burke, M. Ernzerhof, Generalized Gradient Approximation Made Simple, Phys. Rev. Lett. 77 (1996) 3865–3868.

[36] A. Togo, I. Tanaka, First principles phonon calculations in materials science, Scr. Mater. 108 (2015) 1–5.

[37] A. Stukowski, Visualization and analysis of atomistic simulation data with OVITO–the Open Visualization Tool, Modell. Simul. Mater. Sci. Eng. 18 (2010) 015012.

[38] A. Jain, S. P. Ong, G. Hautier, W. Chen, W. D. Richards, S. Dacek, S. Cholia, D. Gunter, D. Skinner, G. Ceder, K. A. Persson, Commentary: The Materials Project: a materials genome approach to accelerating materials innovation, APL Mater. 1 (2013) 011002.

[39] L. Liu, X. Wu, R. Wang, W. Li, Q. Liu, First principle study on the temperature dependent elastic constants, anisotropy, generalized stacking fault energy and dislocation core of NiAl and FeAl, Comput. Mater. Sci. 103 (2015) 116–125.

[40] J. D. Eshelby, The determination of the elastic field of an ellipsoidal inclusion, and related problems, Proc. R. Soc. Lond. Ser. A Math. Phys. Eng. Sci. 241 (1957) 376–396.

[41] J. D. Eshelby, Elastic inclusions and inhomogeneities, Prog. sol. mech. 2 (1961) 89–140.

[42] D. Li, L. Chen, Morphological evolution of coherent multi-variant $Ti_{11}Ni_{14}$ precipitates in Ti-Ni alloys under an applied stress–a computer simulation study, Acta Mater. 46 (1998) 639–649.

[43] Z. K. Lu, G. J. Weng, Two-level micromechanical theory for a shape-memory alloy reinforced composite, Inter. J. Plas. 16 (2000) 1289–1307.

[44] H. Sehitoglu, I. Karaman, R. Anderson, X. Zhang, K. Gall, H. Maier, Y. Chumlyakov, Compressive response of NiTi single crystals, Acta Mater. 48 (2000) 3311–3326.

[45] N. Kinoshita, T. Mura, Elastic fields of inclusions in anisotropic media, Phys. Stat. Soli. (a) 5 (1971) 759–768.

[46] M. Kato, T. Fujii, S. Onaka, Elastic strain energies of sphere, plate and needle inclusions, Mater. Sci. Eng. A 211 (1996) 95–103.

[47] A. Ishii, J. Li, S. Ogata, Shuffling-controlled versus strain-controlled deformation twinning: The case for HCP Mg twin nucleation, Inter. J. Plas. 82 (2016) 32–43.